nature catalysis

Article

https://doi.org/10.1038/s41929-024-01187-4

Key role of paracrystalline motifs on iridium oxide surfaces for acidic water oxidation

Received: 15 August 2023

Accepted: 10 June 2024

Published online: 10 July 2024

Check for updates

Bingzhang Lu[1,5], Carolin Wahl[2,3,5], Roberto dos Reis[2,3], Jane Edgington[1], Xiao Kun Lu[1], Ruihan Li[1], Matthew E. Sweers[2], Brianna Ruggiero[1], G. T. Kasun Kalhara Gunasooriya[4], Vinayak Dravid[2,3] & Linsey C. Seitz[1]

Water electrolysis using proton exchange membrane technology offers an ideal process for green hydrogen production, but widespread deployment is inhibited by insufficient catalyst activity, stability and affordability. Iridium-based oxides provide the best overall performance for acidic water oxidation, the limiting reaction for this process, but further improvements are impeded by poor understanding of the restructured active catalyst surface that forms under reaction conditions. Here we present a combination of X-ray and electron scattering data that reveals direct evidence for three paracrystalline structural motifs at the restructured surfaces of highly active catalysts (including rutile IrO_2 and perovskite $SrIrO_3$) that have previously been described as amorphous. These insights enable the design of a paracrystalline IrO_x catalyst that is independent of the bulk crystalline support and maintains higher activity, longer stability and more effective use of iridium to promote the production of green hydrogen.

Water oxidation, also known as the oxygen evolution reaction (OER), in acidic electrolyte is a critical bottleneck of proton exchange membrane electrolysers for the production of green hydrogen. Beyond hydrogen, the OER also plays a pivotal role in many electrosynthesis processes that will become essential in our pending transition to renewable energy[1–3]. Therefore, a highly active, durable and affordable OER catalyst is one of the most critical targets of modern electrochemistry[4–6]. However, the highly oxidative potentials, strongly acidic conditions and sluggish kinetics greatly limit the choice of catalyst material[7,8]. Among the few available materials, the most promising and studied catalyst systems are primarily iridates (that is, A_xIrO_y, where A is a group I–IIA or IIIB metal)[9,10], many of which display an enhancement in OER activity upon initial electrochemical activation while undergoing surface rearrangement.

Current research directions often aim to enhance activity and stability by tuning bulk crystal phases (for example, 3C-phase cubic perovskites (with ABO_3 stoichiometry, where A and B are cations)[9], 6H-phase hexagonal structures[11], Ruddlesden–Popper series ($A_{n+1}B_nX_{3n+1}$ stoichiometry, where X is an anion)[12], double perovskites ($AA'BB'O_6$ stoichiometry)[10] or pyrochlores ($A_2B_2X_6Y$, where Y is non-stoichiometric X)[13]), substituting alternative A site elements (for example Sr (ref. 14), Li (ref. 15), Ca (ref. 16), Ba (ref. 17) or rare earth metals[18]) or adopting other modifications (for example, incorporating Co (ref.19), Fe (ref. 20) or Zn (ref. 21)). Whereas these approaches have resulted in unique variations in activity and stability, these materials share a common fate of surface IrO_x layer reconstruction and amorphization, providing a range of undefined active sites for the OER. Therefore, the relevant electrocatalytic properties of these iridates are determined by the Ir–O structural motifs within the surface IrO_x layer, instead of the bulk crystals of the pre-catalysts.

This dynamic restructuring during the reaction has made identifying, understanding and optimally harnessing these amorphized IrO_x motifs extraordinarily difficult. Characterizing such materials is challenging due to interference from the electrode substrate or bulk crystalline material, which may obscure the signal from amorphized active site motifs. Furthermore, accurate microscopy of amorphous materials

[1]Department of Chemical and Biological Engineering, Northwestern University, Evanston, IL, USA. [2]Department of Materials Science and Engineering, Northwestern University, Evanston, IL, USA. [3]International Institute for Nanotechnology, Northwestern University, Evanston, IL, USA. [4]School of Sustainable Chemical, Biological and Materials Engineering, University of Oklahoma, Norman, OK, USA. [5]These authors contributed equally: Bingzhang Lu, Carolin Wahl. e-mail: linsey.seitz@northwestern.edu

https://doi.org/10.1038/s41929-024-01187-4

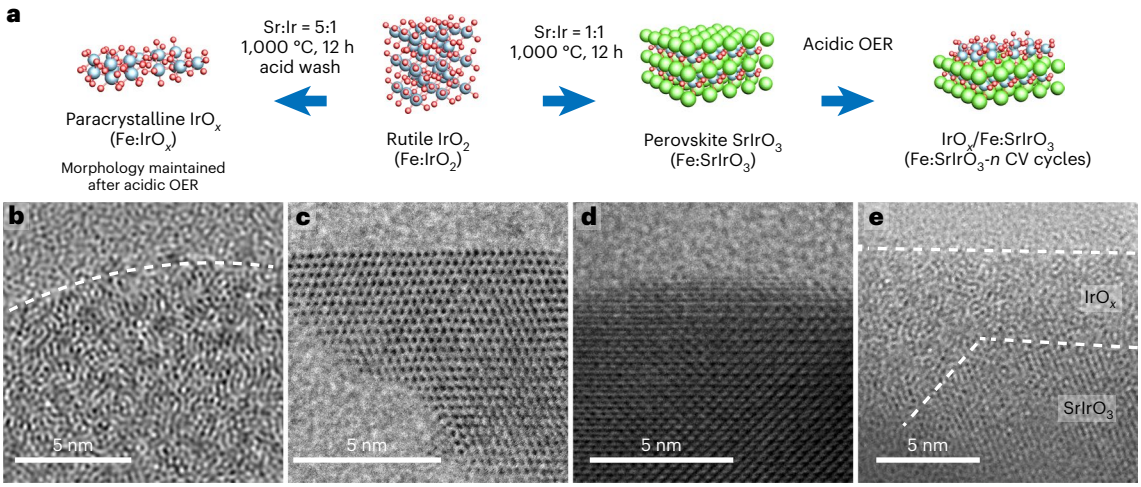

Fig. 1 | Microscopy studies of catalysts derived from iridates. a, Schematic illustration of material syntheses. Rutile Fe-doped IrO_2 (Fe:IrO_2) is used as both a sample and the precursor for other samples. Perovskite Fe:$SrIrO_3$ was obtained with Sr:Ir = 1:1 via a calcination method and is shown to experience surface amorphization and reconstruction during the OER process. Paracrystalline Fe:IrO_x was obtained with excess Sr via calcination and acid washing; its pristine morphology is maintained after OER testing. Atom colours: Ir, blue; O, red; Sr, green. **b**–**e**, Fourier-filtered annular bright-field STEM images of paracrystalline Fe:IrO_x (**b**), rutile Fe:IrO_2 (**c**), perovskite Fe:$SrIrO_3$ (**d**) and surface-amorphized IrO_x/Fe:$SrIrO_3$ (**e**). Dashed lines in **b**,**e** are shown to highlight the catalyst surface versus the background or interface between amorphized surface layer and bulk crystalline material.

is particularly difficult due to a lack of high-sensitivity direct electron detectors, without which, beam-induced damage causes unpredictable transformations such as crystallization[22,23], forming structures that do not represent the active catalyst. Consequently, current knowledge and insights have primarily been limited to confirming the existence of a nominal amorphous Ir-enriched surface layer[24,25], whereas few other studies have proposed possible Ir–O structural motifs (for example, corner-[17] or face-shared octahedra[11], rutile[26], hollandite[25], honeycomb[22] and so on). However, direct or systematic experimental evidence of these structural motifs within the amorphized IrO_x layer and their structure–function relationships have remained elusive. Theoretical studies have assessed the performance and properties of several proposed Ir–O structures, but these insights are still limited by the massive computational power needed to assess the sheer number of possible structures[27] and debated reaction mechanisms[28]. Furthermore, the ability to stabilize these highly active IrO_x motifs without needing a bulk crystalline material to support surface restructuring and provide long-term stability is a promising approach to enable enhanced performance and utilize platinum group metals effectively.

We present direct evidence of short-to-medium-range-order (7–9 Å) paracrystalline structures for the previously described amorphized IrO_x surface layers formed on $SrIrO_3$ perovskites upon driving the OER under acidic conditions. We leverage a unique combination of advanced characterization techniques, including the localized electron pair distribution function (ePDF) through four-dimensional scanning transmission electron microscopy (4DSTEM), the X-ray scattering pair distribution function (xPDF) and extended X-ray absorption fine-structure (EXAFS) spectroscopy, to gather clear evidence for three fundamental [Ir–O_6] octahedral connection types that comprise these highly active IrO_x materials. Furthermore, we stabilize paracrystalline IrO_x nanoparticles with motifs that are highly similar to amorphized IrO_x/$SrIrO_3$ surfaces after the OER, and we exhibit excellent OER performance, long-term stability and improved Ir utilization without the need for a bulk crystalline support material. The results presented here address many long-standing questions regarding the structure, active sites, dynamics and chemical properties of highly active IrO_x structural motifs derived from crystalline materials, such as perovskite $SrIrO_3$, synthesized here in powder form via Fe doping. Finally, this study opens research avenues into paracrystalline IrO_x materials and demonstrates the application of advanced electron-scattering-based methods to carefully examine such materials, providing valuable insights for the next generation of electrocatalysts.

Results

Catalyst synthesis and structural analysis

$SrIrO_3$ perovskite and paracrystalline IrO_x nanoparticles were synthesized using a modified calcination synthesis starting from rutile IrO_2 nanoparticles (Fig. 1a,c and Supplementary Figs. 1 and 2). Fe was included (at an Fe:Ir ratio of 1:4) as a critical phase-selection agent (characterization of Fe is included in Supplementary Note 10) to synthesize the crystalline 3C perovskite (that is, Fe-doped $SrIrO_3$ (Fe:$SrIrO_3$); Fig. 1a,d and Supplementary Figs. 3 and 4), and excess Sr precursor was used (at an Sr:Ir ratio of 5:1) to achieve the uniform paracrystalline patterns shown in Fig. 1a,b and Supplementary Figs. 5–8 for Fe-doped IrO_x (Fe:IrO_x). The paracrystallinity of Fe:IrO_x is highly consistent with the surface IrO_x of the $SrIrO_3$ perovskite nanoparticles after OER testing for 2,000 cyclic voltammetry (CV) cycles (Fe:$SrIrO_3$-2,000; Fig. 1e and Supplementary Figs. 9–12), but Fe:IrO_x itself does not exhibit any obvious morphological change after the OER (Supplementary Figs. 13–15). (See Supplementary Note 1 for additional microscopy studies.)

Without signal interference from a traditional bulk iridate crystal beneath a surface-amorphized active catalyst layer, paracrystalline Fe:IrO_x enables a combination of xPDF studies derived from X-ray total scattering and EXAFS spectral analysis to reveal the structure of Fe:IrO_x directly (Fig. 2a,b). First, the broad scattering ring (Fig. 2a) and resulting xPDF—denoted by $G(r)$—with features limited to 7–9 Å or shorter highlight the short-range-order paracrystalline structure of Fe:IrO_x that parallels our electron microscopy image (Supplementary Fig. 5). By comparison, crystalline materials (that is, Fe:$SrIrO_3$ and Fe:IrO_2) exhibit sharper scattering rings and $G(r)$ peaks over longer ranges, whereas completely amorphous materials exhibit $G(r)$ peaks over distances shorter than 4 Å (ref. 28). Second, three main $G(r)$ peaks are identified for Fe:IrO_x at 2.00 Å (Ir–O), 3.09 Å (Ir–Ir edge) and 3.57 Å (Ir–Ir corner with ∠Ir–O–Ir ≈ 128°); from Fourier-transformed EXAFS data, the corresponding coordination numbers (CNs) are fitted at 6.06, 4.36 and 4.38, respectively. These path lengths and associated CNs identify the basic unit structures as [Ir–O_6] octahedra that share edges or corners and limit the possible structures to only three types of connection, referred to here as type I, II and III (Fig. 2d and Supplementary Figs. 16 and 17). These results exclude some important structural candidates,

https://doi.org/10.1038/s41929-024-01187-4

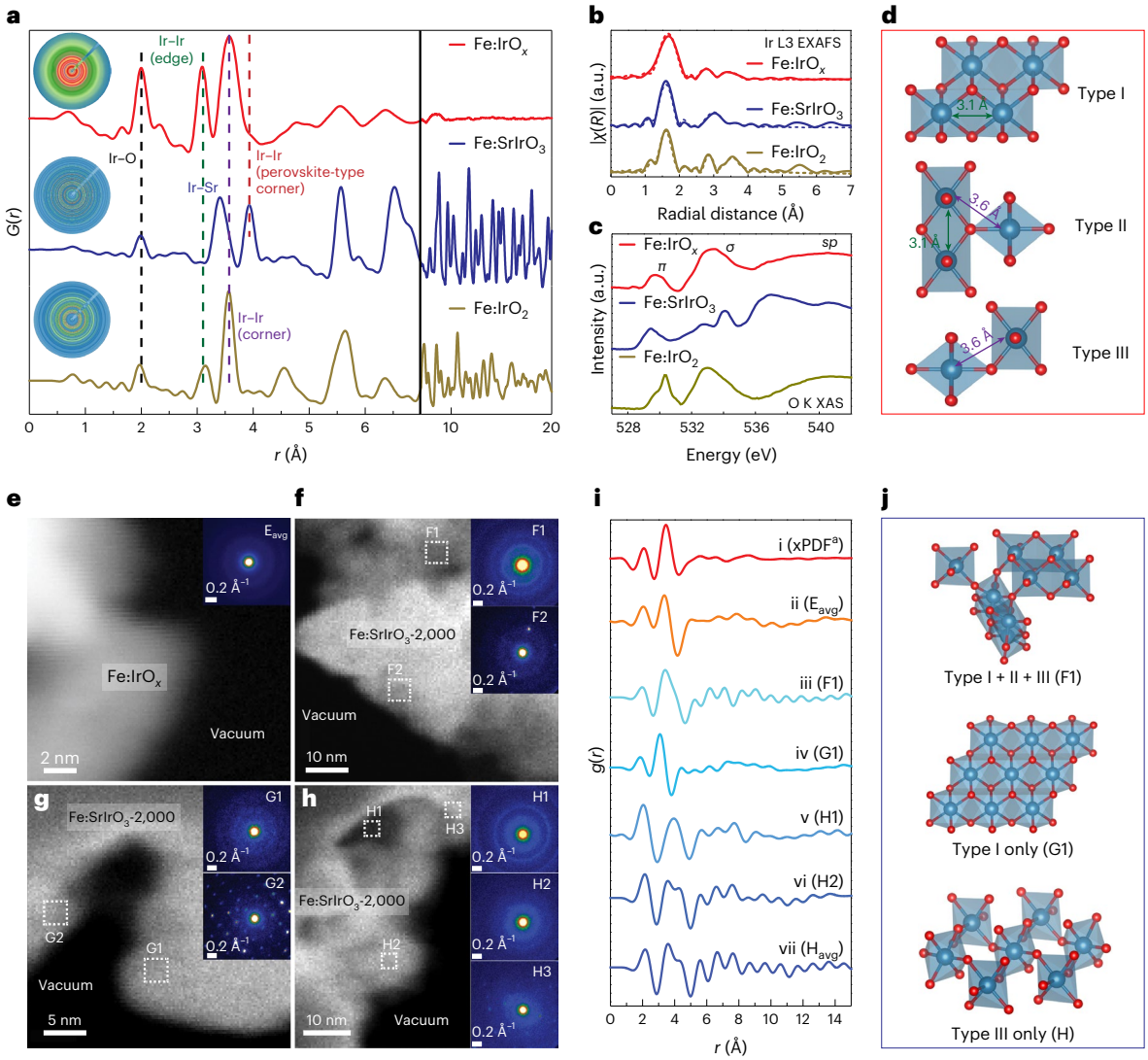

Fig. 2 | Characterization of catalysts derived from iridates. a, xPDF $G(r)$ functions, with X-ray total scattering patterns shown as insets. **b**, Iridium L3-edge Fourier-transformed EXAFS data. **c**, Oxygen K-edge XAS data. **d**, Schematic illustration of the three identified [Ir–O_6] octahedral connection types of paracrystalline Fe:IrO_x with Ir–Ir bond lengths. Colours of arrows and labels match the identified xPDF $G(r)$ peaks in **a**. **e**–**h**, Virtual annular dark-field STEM images reconstructed from 4DSTEM datasets with diffraction patterns shown as insets. The inset in **e** shows the averaged diffraction pattern over the whole field of view for Fe:IrO_x. The insets in **f**–**h** show the diffraction patterns for the amorphized surface of Fe:$SrIrO_3$-2,000 averaged over the marked square boxes; note that regions F2, G2 and H3 are deeper within the sample and show features from the bulk crystal. **i**, The ePDF $g(r)$ functions associated with **e**–**h**. [a]Curve i shows the same xPDF data as in **a** but with truncated resolution for direct comparison with the ePDF results (curves ii–vii). **j**, Schematic illustration of the three local structures found in the amorphized surface of Fe:$SrIrO_3$-2,000.

such as the corner-sharing perovskite-type structure (∠Ir–O–Ir ≈ 180°) or face-sharing octahedra, rutile-, brookite-, pyrite-, columbite- and anatase-type motifs as they do not match the analysed structures (Supplementary Figs. 18–20)[29].

Consistent with several previous hypotheses, we find that hollandite or romanechite contain some similar structural motifs[25,28,30] but are still not an exact match. (Supplementary Note 2 includes an extended discussion on the identification and exclusion of the respective structures.) Oxygen K-edge X-ray absorption spectroscopy (XAS; Fig. 2c) shows that Fe:IrO_x has a broad e_g feature without sharp peaks, which also indicates a highly disordered structure and excludes rutile, brookite and anatase crystal patterns, consistent with previous observations[25].

For electrolysis, the samples are mixed with various forms of carbon that contribute scattering signals; these signals interfere with structural analysis, precluding use of the above-mentioned techniques to analyse the cycled materials and thus presenting a major difficulty in many studies of iridate OER catalysts. By comparison, the spatially localized electron probe of ePDF enables the region-specific/selective study of the catalyst material without interference from its support. However, amorphous and paracrystalline structures are extremely sensitive to electron irradiation: incoming electrons immediately reduce the IrO_x and nucleate metallic Ir clusters that grow into nanoparticles under continued irradiation. This damage process occurs rapidly under typical imaging conditions, and substantial crystallization is already present in the first acquired image, such that the electron beam-induced damage can go entirely unnoticed (Supplementary Figs. 21–24 and Supplementary Videos 1–3). For ePDF studies in this work, special care was taken to minimize radiation damage; data were collected using fast electron detectors (~20,000 frames per s) and low electron currents on previously unexposed sample areas (Supplementary Note 3). In doing this, we disclose the rearranged local surface structure of OER-tested Fe:$SrIrO_3$-2,000 and prove its structural similarity to the as-synthesized Fe:IrO_x. Figure 2e shows the uniform

https://doi.org/10.1038/s41929-024-01187-4

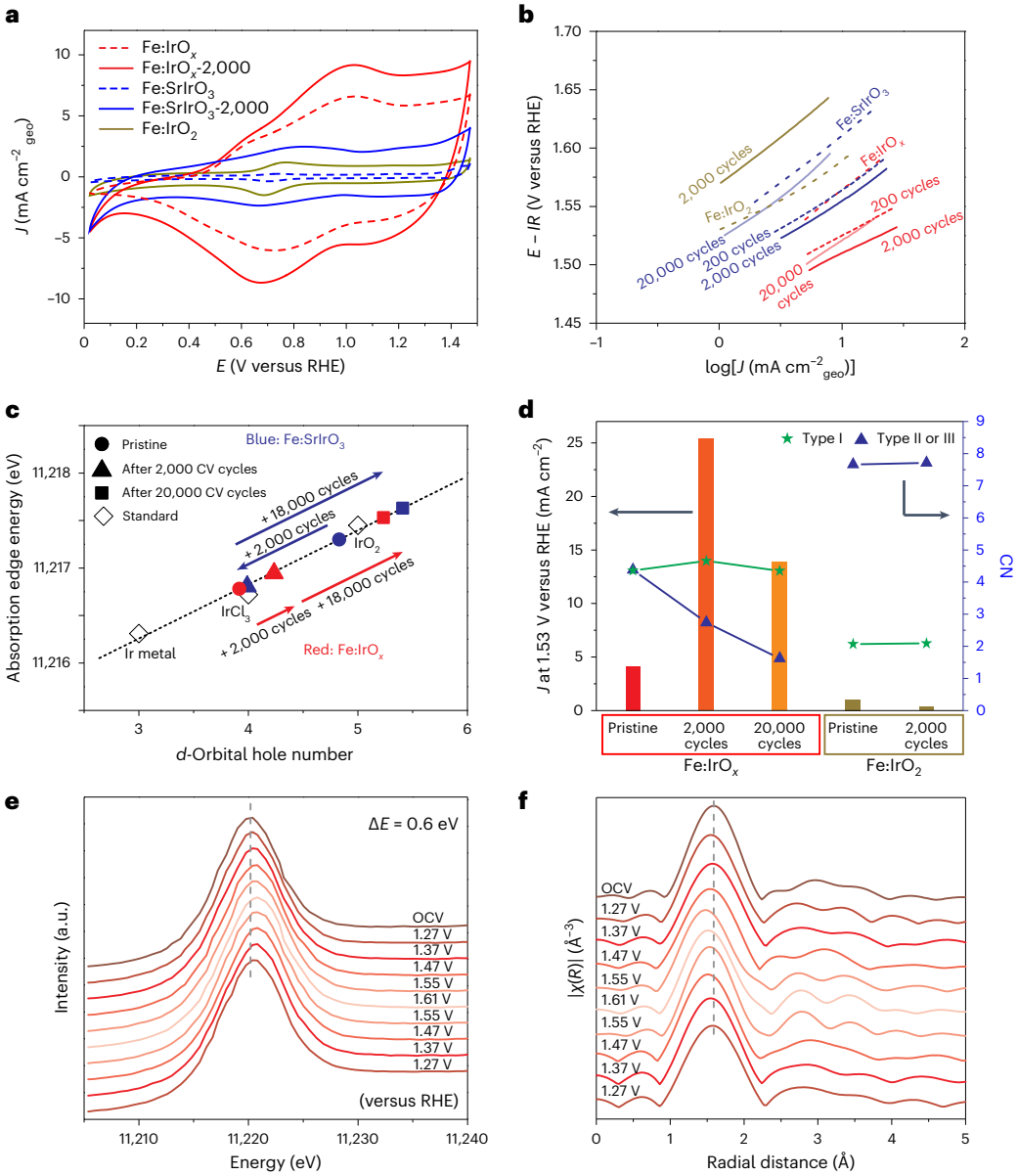

Fig. 3 | Evolution of electrochemical performance and XAS. a, Cyclic voltammograms in the non-Faradaic region. **b**,**c**, Tafel plots (**b**) and summarized XAS edge positions (**c**) of the catalysts at various stages of OER testing. In **b**, the curves are *iR*-corrected (*I*, current; *R*, series resistance). **d**, Summarized activity (bars) and change in Ir–Ir CN (filled symbols) for paracrystalline Fe:IrO_x and rutile Fe:IrO_2. **e**,**f**, In situ XAS (**e**) and in situ EXAFS (**f**) of paracrystalline Fe:IrO_x-2,000 as a function of the applied potential *E*. OCV, open-circuit voltage.

diffraction ring pattern detected across the whole field of view, resulting in an ePDF—denoted by $g(r)$—that shows excellent agreement with the resolution-truncated xPDF results for Fe:IrO_x (Fig. 2i(i),(ii)). This ePDF-derived $g(r)$ function reveals two major peaks at 2.00 Å (Ir–O bond) and 3.35–3.45 Å; the latter represents a convolution of the 3.10 Å and 3.60 Å Ir–Ir path lengths that appear as separate peaks in the higher resolution xPDF. This ePDF–xPDF comparison reveals local and broad homogeneity of Fe:IrO_x and supports the robustness of the following measurements.

Examining the rearranged surface IrO_x layer of the perovskite catalyst after 2,000 CV cycles of OER testing (Fe:$SrIrO_3$-2,000), we map the spatial distribution of crystalline and paracrystalline regions (Supplementary Figs. 25 and 26) and identify three representative local structures in these paracrystalline regions. Figure 2f–h highlights various paracrystalline zones (F1, G1, H1 and H2) with clear diffraction rings that translate into $g(r)$ functions, in addition to mixed paracrystalline and crystalline zones (F2, G2 and H3) that feature long-range ordering manifesting as well-resolved diffraction patterns (Supplementary Fig. 25). The $g(r)$ functions in Fig. 2i(iii)–(vii) and Supplementary Fig. 27(iii)–(vii) are derived from regions within the surface IrO_x layer of Fe:$SrIrO_3$-2,000 and show signal termination at 7–9 Å, exhibiting the same degree of paracrystallinity across these IrO_x structural motifs. Peaks at ~2.0 Å are consistent across the samples and are indicative of their invariant Ir–O bonds, whereas the varying positions of the Ir–Ir peaks reflect their structural differences. Zone F1 shows a convoluted Ir–Ir peak at 3.4 Å, indicating a very similar structure to Fe:IrO_x (that is, containing type I + II + III connections; Fig. 2j), whereas zone G1 exhibits a type-I-only structure, identified by the 3.1 Å peak. Moreover, zones H1, H2 and H average (H_{avg}) all show peaks at 3.6, 4.3 and 5.6 Å, consistent with the type-III-only structure (Supplementary Fig. 28) and similar to the theoretically proposed R-IrO_3 or α-IrO_3 structures[27,28].

Fe:IrO_x and the surface of Fe:$SrIrO_3$-2,000 are highly similar yet have observable differences: they both exhibit paracrystallinity with the same range order and the same three types of [Ir–O_6] octahedral

connection; although much of the local structure is identical, Fe:IrO_x shows a homogeneous combination of the three connection types, whereas the Fe:$SrIrO_3$-2,000 surface layer exhibits some heterogeneity, with type-I-only or type-III-only zones observed in some regions (Supplementary Fig. 29).

Structural evolution and active site identification

Electrochemical analysis was conducted to assess the short- and long-term electrochemical performance and dynamic behaviour of these materials. Figure 3a reveals a large double-layer capacitance for Fe:IrO_x, several times greater than Fe:$SrIrO_3$ and Fe:IrO_2, which contributes to its high OER activity (Supplementary Figs. 30 and 31). The capacitance of all of the materials increases upon repeated cycling from 1.22 to 1.77 V versus the reversible hydrogen electrode (RHE) (Supplementary Fig. 32). Moreover, these materials exhibit similar activity trends during cycling with an initial increase in activity until a maximum performance is reached, followed by a slow decay (Fig. 3b and Supplementary Fig. 32). Notably, Fe:IrO_x exhibits the best activity among all of the samples, achieving a current density (J) that is around sixfold and ~25-fold higher (at 1.53 V) compared with Fe:$SrIrO_3$ and Fe:IrO_2, respectively, with a smaller OER charge-transfer resistance and a slower activity decay at high cycle numbers (Supplementary Figs. 33 and 34). Fe:IrO_x retains considerable activity, even after 20,000 CV cycles, whereas Fe:$SrIrO_3$ shows a major performance loss; Fe:IrO_2 loses almost all activity within only 2,000 CV cycles. The mass-normalized current density of Fe:IrO_x is around fourfold greater than Fe:$SrIrO_3$. Normalizing by capacitance, both materials exhibit a slightly higher intrinsic activity than rutile IrO_2 (Supplementary Fig. 35), indicating that some of the identified structural motifs in Fe:IrO_x and at the surface of OER-tested Fe:$SrIrO_3$ exhibit superior activity compared with the rutile structure. Electron microscopy studies show that the overall morphology of Fe:IrO_x does not change substantially after 2,000 or even 20,000 CV cycles (Supplementary Fig. 36); the ePDF results of Fe:IrO_2-2,000 also show a highly similar $g(r)$ function compared with pristine Fe:IrO_x (Supplementary Fig. 37). These findings suggest that these materials are not likely to produce any additional structural motifs beyond the three identified connection types.

XAS of the materials before and after electrochemical stability testing revealed a change in the Ir valence state (Fig. 3c, Supplementary Figs. 38–43 and Supplementary Table 1). The initial Ir valence state of Fe:IrO_x is close to Ir^{3+} but increases upon OER cycling and reaches higher than Ir^{4+} at 20,000 CV cycles, possibly generated via gradual structural fragmentation or Ir vacancies. Fe:$SrIrO_3$ shows a high initial Ir valence state of Ir^{4+}, which then decreases to Ir^{3+}, matching the pristine Fe:IrO_x material and consistent with a previous observation[25]. Following surface amorphization, the Fe:$SrIrO_3$ sample closely matches Fe:IrO_x, and shows a similar increase in Ir valence state through subsequent catalyst ageing.

Besides the chemical state, the CN before and after OER stability testing is another key indicator of structural changes (Fig. 3d, Supplementary Figs. 44 and 45 and Supplementary Tables 2–5). All Ir–O CNs are six, indicating that [Ir–O_6] octahedra are still the basic building unit, even after extended OER testing. Nonetheless, the various identified connection types exhibit different responses during catalyst ageing. Type I connections exhibit minimal change, with a consistent value of CN ≈ 4.4–4.7 for the Fe:IrO_x samples at all time points during testing, showing the high stability of this motif. Conversely, type II/III connections exhibit much less stability, with CNs that notably decrease from 4.38 to 2.74 after 2,000 CV cycles and to 1.62 after 20,000 CV cycles. During extended testing, the degradation of type II connections may lead to structural fragmentation, increased Ir valence states (Supplementary Table 6), the formation of surface Ir vacancies (Supplementary Fig. 46) or transformation to type III connections. After an extended time period, degradation of type II/III connections may also cause Ir leaching or conductivity loss, contributing to eventual activity decay. This finding is also consistent with the notably lower stability of reference sample Fe:IrO_2, which has exclusively type II connectivity (Supplementary Fig. 47).

In situ XAS also reveals uniquely reversible properties for Fe:IrO_x during OER cycling, featuring a gradual increase in the Ir valence state to Ir^{4+} and a contraction of the Ir–O bond (~2.5% from 2.01 to 1.96 Å) while maintaining CN = 6 at increasingly oxidative potentials (Fig. 3e,f, Supplementary Figs. 48 and 49 and Supplementary Tables 7 and 8). On returning to less oxidative potentials, these properties revert to their earlier states. This reversible behaviour persists after 20,000 CV cycles but is slightly weaker (Supplementary Fig. 50), correlating with the small activity loss over time. Interestingly, these reversible dynamics are not observed during the very first cycles of pristine Fe:IrO_x, when it exhibits a slightly lower initial activity (Supplementary Fig. 51), perhaps due to a more interconnected and inflexible structure. By comparison, no obvious change in the valence state or bond length with cycling can be observed in the fully crystalline Fe:$SrIrO_3$ and Fe:IrO_2 samples (Supplementary Figs. 52 and 53). We hypothesize that the paracrystalline nature of the Fe:IrO_x catalyst enables this dynamic valence state and bond length, which appears to be crucial to its high performance. An overview of the dynamic stability observed for these materials and an illustration of the proposed structural evolution is included in Supplementary Note 8.

Density functional theory (DFT) calculations were used to further assess the properties of the experimentally identified catalyst motifs and elucidate their structure–activity relationships. Owing to the complexity of modelling the active site motifs of the actual paracrystalline materials, we selected crystalline materials that closely resemble the three connection types and calculated the theoretical OER overpotential (η_{OER}) values for stable active site motifs (Fig. 4a–f, Supplementary Tables 9–12 and model details in Supplementary Note 7). We consider both pristine structures and those with Ir vacancies to represent the paracrystallinity of these materials. Figure 4g shows the calculated η_{OER} values of different active site models using the adsorbate evolving mechanism (AEM; Fig. 4i, top) that proceeds through adsorbed hydroxyl (OH*), oxygen (O*) and peroxo (OOH*) species (Supplementary Fig. 54)[6,31]. The type I motif is best represented by birnessite. The Ir sites on birnessite (001) surfaces have a weak OH* adsorption energy, resulting in poor activity (η_{OER} = 1.32 V; Fig. 4a), but the edge sites of birnessite (100) exhibit comparatively enhanced activity (η_{OER} = 0.87 V; Fig. 4b). By comparison, the Ir sites of type II/III connections show high activities: type II motifs (rutile; Fig. 4c) and type III motifs (IrO_x; Fig. 4d) exhibit low overpotentials of 0.59 V and 0.66 V, respectively. Similarly, the edge site motifs of hollandite (100) (Fig. 4e and Supplementary Fig. 55), romanechite (100) (Fig. 4f and Supplementary Fig. 55) and romanechite (001) (Supplementary Fig. 55) contain Ir sites with type II connections that have high predicted OER activities (η_{OER} = 0.57, 0.46 and 0.73 V, respectively). These theoretical studies further support our hypotheses that the high activity of these materials is more strongly related to type II/III connections than type I, although these crystalline material models do not perfectly match the paracrystalline structure identified experimentally.

Iridium vacancies were also introduced to the calculated structures to represent incomplete crystallinity in these materials. Generally, defected structures with Ir vacancies have higher Ir valence states, with some approaching Ir^{5+} (Supplementary Table 13). From the viewpoint of the stability, birnessite (001) has the highest Ir vacancy formation energy of 5.38 eV (Supplementary Table 14), indicating a high energy barrier to creating vacancies and causing fragmentation of these structures, further confirming the experimental results that indicate the high stability of type I motifs. From the viewpoint of the activity, defect-containing birnessite has a slight activity enhancement compared with pristine birnessite, whereas defect-containing rutile, hollandite and romanechite show more diversity of activity, with some sites exhibiting very high activity for the OER (Supplementary Figs. 55

https://doi.org/10.1038/s41929-024-01187-4

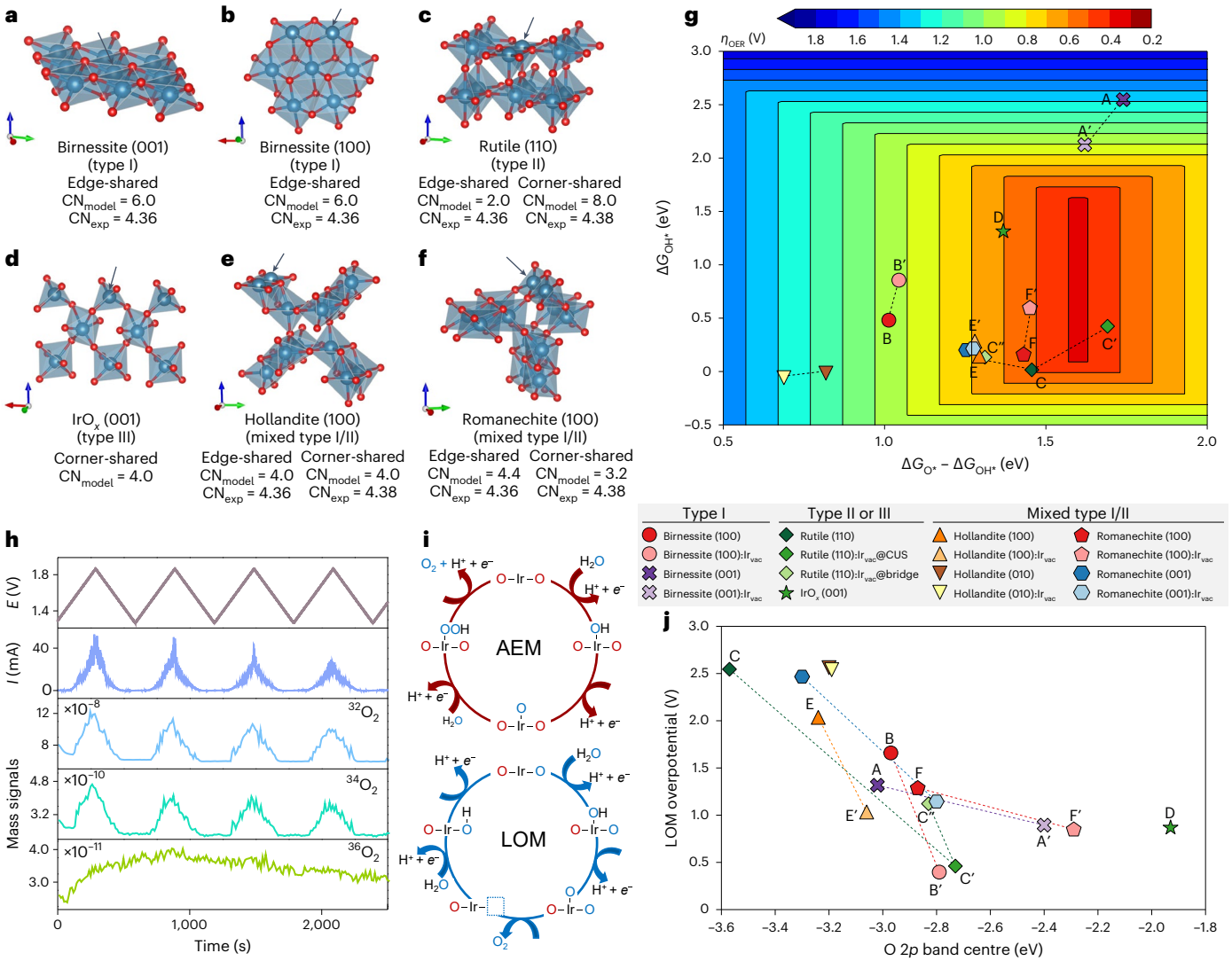

Fig. 4 | OER theoretical analysis. a–**f**, Structural models of birnessite (001) (**a**), birnessite (100) (**b**), rutile (110) (**c**), IrO_x (001) (**d**), hollandite (100) (**e**) and romanechite (100) (**f**) used for DFT investigations to represent type I, II and III connections. Atom colours: Ir, blue; O, red. Black arrows identify the active sites considered for the OER. CN_{model}, simulated CN; CN_{exp}, measured CN. **g**, Two-dimensional OER activity plot of the theoretical overpotential (η_{OER}) values for the active site models (corresponding to **a**–**f** in this study) as a function of $\Delta G_{O^*} - \Delta G_{OH^*}$ and ΔG_{OH^*} using the AEM. The contour map is constructed using the scaling relation of $\Delta G_{OOH^*} = \Delta G_{OH^*} + 3.2$ eV. Ir_{vac}, Ir vacancy site; Ir_{val}@CUS, Ir vacancy at a coordinatively unsaturated site; Ir_{val}@bridge, Ir vacancy at a bridge site. **h**, Differential electrochemical mass spectrometry study of Fe:IrO_x-2,000. *I*, current. **i**, Schematic representation of the possible OER mechanisms considered in this study: AEM (top) and LOM (bottom). $H^+ + e^-$, proton-coupled electron transfer (PCET) step. **j**, Correlation between the computed OER LOM overpotential and the O 2*p* band centre for selected motifs, where the key to the motifs is the same as in **g**.

and 56). For example, romanechite (100):Ir_{vac} (motif F′ in Fig. 4g) exhibits a substantially lower overpotential of 0.39 V. This indicates that the fragmentation of long-range crystal structures into short-range motifs, elevated Ir oxidation states and the high structural diversity of these materials support highly active reaction sites, and are key features of high-performance IrO_x OER catalysts.

Monitoring the mass of evolved O_2 from Fe:IrO_x labelled with ^{18}O reveals the formation of $^{32}O_2$ and $^{34}O_2$, while $^{36}O_2$ is absent (Fig. 4h and Supplementary Fig. 57); this indicates the existence of the single-vacancy lattice oxygen mechanism (LOM; Fig. 4i, bottom, and Supplementary Fig. 58), which is also observed in Fe:$SrIrO_3$-2,000 samples (Supplementary Fig. 59). Examining the OER activity of the surface models using the LOM (Fig. 4j), we found that most of the pristine surfaces are predicted to have limited LOM activity due to high oxygen coupling energies. However, with the introduction of Ir vacancies (Fig. 4i,j), there is a substantial positive shift of the O 2*p* band centre for all structures, consistently inducing an enhancement in the LOM activity. For example, LOM activation on birnessite edge sites reduces the η_{OER} from 1.66 to 0.40 V (Supplementary Fig. 55), demonstrating that these fragmented oxide structures can support highly active sites through the LOM as well.

Conclusions

Through the systematic characterization of Fe:IrO_x and perovskite Fe:$SrIrO_3$, we have brought understanding to the highly active amorphized IrO_x surface layers that evolve under reaction conditions from crystalline iridates. These highly active structural motifs consist of short-range-order [Ir–O_6] octahedra with three basic connection types; the identified type I connections probably provide enhanced stability and the type II/III connections primarily contribute to high activity via both AEM and LOM pathways. The structural diversity and paracrystalline nature of these materials support the dynamic stability observed as these catalysts are resilient to changes in Ir valence state and Ir–O bond lengths with changes in potential and extended cycling. As a

result, Fe:IrO_x exhibits a much slower activity decline compared with commonly investigated crystalline catalysts such as rutile IrO_2 and iridate perovskites.

Through this work, we have monitored and mitigated electron-beam-induced crystallization, which has been a poorly defined yet critical issue for amorphous and paracrystalline materials, to establish a minimal-dose workflow for damage-free imaging. This work also introduces the comprehensive characterization of complex electrocatalysts via a combined XAS–xPDF–ePDF experimental workflow, enabling both local and global characterization, which is critical for understanding catalyst evolution before and after electrochemical testing. These discoveries answer long-standing questions about structure, activity, stability and degradation processes for iridate catalysts. We have also applied this understanding and developed a synthesis method for paracrystalline materials that exploits controlled calcination and elemental leaching to generate catalysts that stabilize these highly active paracrystalline structural motifs, without the need for bulk material support. This approach enables a substantially enhanced surface area and the utilization of platinum group metals, perhaps paving the way for the next generation of dynamically stable OER catalysts.

Methods

Synthesis of rutile Fe:IrO_2 nanoparticles

Fe:IrO_2 nanoparticles were synthesized through a template method using SBA-15 mesoporous silica. SBA-15 with a pore size of 10 nm was prepared on the basis of previous work[32]. $IrCl_4$ (175 mg) and $Fe(NO_3)_3{\cdot}9H_2O$ (70 mg) were fully dissolved in ethanol (5 ml) with several drops of HCl. Next, SBA-15 (60 mg) was added to the solution and sonicated for 2 h to achieve a homogeneous solution. This solution was then placed in an oven at 40 °C overnight to evaporate the solvent. The mixture was then heated at 500 °C for 2 h in a box furnace. After that, the black powder was washed several times by dispersion in 2 M NaOH and heating to 90 °C for 1 h to remove the SiO_2 template.

Synthesis of paracrystalline Fe:IrO_x

In a typical synthesis, Fe:IrO_2 (30 mg) was dispersed in H_2O (15 ml) and sonicated until a homogeneous solution was formed. Next, a 5 ml volume of an aqueous solution of polyvinylpyrrolidone (300 mg) and a 5 ml volume of an aqueous solution of $Sr(NO_3)_2$ (141 mg) were added to the previous solution under stirring. Then, 5 ml of an aqueous solution with Na_2CO_3 (71 mg) was added dropwise under vigorous stirring. The solution was stirred for an extra 2 h to achieve complete reaction, followed by centrifugation at 6,000 revolutions per min. The obtained black-grey powder was placed in a box furnace and heated to 1,000 °C for 12 h. Then, the powder was carefully dissolved in 0.18 M HCl (10 ml) and sonicated for 5 min. Finally, the solution was centrifuged at 9,000 revolutions per min for 5 min, followed by washing with water twice.

Synthesis of perovskite Fe:$SrIrO_3$

The synthesis process is similar to Fe:IrO_x, except that $Sr(NO_3)_2$ (28.2 mg) and Na_2CO_3 (14.2 mg) were used. After calcination, the sample did not undergo an acid-washing process.

Electrochemical measurements

Electrochemical measurements were carried out using a BioLogic VSP electrochemical workstation with a conventional three-electrode configuration. A Ag/AgCl electrode with 4 M KCl was adopted as the reference electrode and a platinum wire coil acted as the counter electrode. The experiments were carried out in 0.1 M $HClO_4$. To prepare the catalyst inks, the catalyst (2 mg) was homogeneously suspended in ethanol (200 µl) and Nafion 117 solution (2 µl) (Aldrich, 5%) under sonication. A 50 µl portion of the resulting ink was dropcast on to a carbon paper sheet (Toray, TGP-H-060) with an area of 1 × 1 cm.

Electron microscopy studies and ePDF

STEM images were acquired using a JEOL ARM200CF, aberration-corrected S/TEM instrument equipped with cold field-emission gun operated at 200 kV and a hexapole probe aberration corrector (CEOS). The convergence semi-angle used in STEM mode was set to 20.6 mrad; the collection semi-angle for high-angle annular dark-field imaging ranged from 90 to 370 mrad and for annular bright-field imaging it ranged from 10 to 23 mrad. The probe current was set to 5 pA for a probe size of 1.28 Å. The electron dose rate for STEM imaging was 6.28×10^6 electrons per s. Energy-dispersive spectroscopy data were collected using a low-background beryllium holder and dual silicon drift detectors with the area of a single detector covering 100 mm^2. The achievable solid angle for energy-dispersive spectrum analysis was around 1.7 sr. The probe current for energy-dispersive spectroscopy was set to 35 pA with a probe size of 1.34 Å. TEM images were acquired using a JEOL ARM300F S/TEM instrument equipped with a cold field-emission gun operated at 300 kV.

Supplementary Videos 1–3 were generated from drift-corrected three-frame rolling averages using Protochips AXON software (www.protochips.com).

The 4DSTEM technique was used in this study to investigate the local atomic structure of the material via the ePDF. The 4DSTEM data were collected using the JEOL ARM300F microscope operated at 80 kV in STEM mode and equipped with a Gatan/DECTRIS Stela, a hybrid pixelated electron detector. 4D arrays (x, y, Qx, Qy) were collected with (128, 128, 512, 512) pixels and a pixel time acquisition of 0.4 ms, resulting in a total dose of 2.6×10^5 electrons per dataset. The convergence semi-angle (α) was set to 0.74 mrad.

To extract the ePDF from the 4DSTEM data[33], the radially averaged intensity of the two-dimensional diffraction patterns was first calculated using in-house Python codes. The total scattering structure function, $S(q)$, was obtained using equation (1):

$$S(q) = \int I(Qx, Qy)\,\mathrm{d}\Omega / \int I_0(Qx, Qy)\,\mathrm{d}\Omega \tag{1}$$

where $I(Qx, Qy)$ represents the diffraction pattern intensity at the coordinates (Qx, Qy), Q is the magnitude of the scattering vector $Q = (Qx^2 + Qy^2)^{1/2}$, $\mathrm{d}\Omega$ is the differential solid angle over which the integration is performed and $I_0(Qx, Qy)$ is the unscattered beam intensity, used as a normalization factor to account for variations in beam intensity.

Next, the reduced structure function $F(Q)$, was calculated as the ratio of the total scattering structure function ($S(Q)$) to the atomic factor $f(Q)$, which accounts for the scattering amplitude of an isolated atom as a function of Q, as in equation (2):

$$F(Q) = S(Q)/f(Q). \tag{2}$$

The ePDF, $g(r)$, was then computed using the inverse Fourier transform of $F(Q)$ as in equation (3):

$$g(r) = (1/2\pi) \int [F(Q) - 1] \times \exp(iqr) \times Q\,\mathrm{d}Q \tag{3}$$

where i is the imaginary unit and r is the real-space vector. This transformation enables the conversion of the reciprocal-space information into real space, providing a quantitative description of the local atomic arrangements. The ePDF analysis was performed for various regions of interest within the sample, highlighting unique features such as the crystal lattice, local disorder and subtle structural variations.

X-ray absorption

Iridium L3-edge data were collected at beamline 5-BM-D of the Advanced Photon Source at Argonne National Laboratory. XAS data

analysis and background-subtraction normalization were carried out using the Demeter program pack[34]. EXAFS data were analysed using the Artemis program. The valence states were estimated via the edge positions, which were determined by the zero-crossing of the second derivative[35–37]. The whiteline peak intensity for these samples can be impacted by self-absorption, whereas the edge energy is not. EXAFS data were fitted with CIF (crystallographic information file) data from rutile IrO_2 (no. 2,723) and perovskite $SrIrO_3$ (no. 1,016,848) from the Materials Project[38]. The R-space fittings were performed using k, k^2 and k^3 weightings. The amplitude reduction factor (S_0^2) was 0.81, determined by fitting standard Ir, IrO_2 and Sr_2IrO_4 samples.

In situ XAS measurements

In situ XAS measurements were carried out for carbon paper-based electrode samples that were previously tested in the laboratory for various numbers of OER CV cycles (0, 2,000 and 20,000). This enabled analysis of samples that had been tested for varying amounts of time, while exposed to actual reaction conditions, without running multiple days-long stability tests at the beamline. The carbon paper working electrodes were placed in a 1 × 1 cm window of a container with 0.1 M $HClO_4$ as the electrolyte. The edges of the carbon paper were sealed using Kapton tape to prevent electrolyte leakage. A piece of copper tape connected the carbon paper electrode and electrochemical workstation. A Ag/AgCl half-cell and a coiled platinum wire were placed in the electrolyte as the reference and counter electrodes, respectively. XAS measurements were executed under various applied electrical potential bias values, both before and after OER onset to examine a range of conditions, including the reaction conditions.

X-ray total scattering and xPDF

The X-ray total scattering data were collected at beamline 11-ID-B of the Advanced Photon Source at Argonne National Laboratory. The $G(r)$ function was exacted using the GSAS-II package[39] and processed using the PDFgetX3 and PDFgui packages[40,41].

Differential electrochemical mass spectrometry

Catalysts were dropcast on to a glassy carbon electrode and isotope labelled by scanning three CV cycles at 1.2–1.6 V versus the Ag/AgCl reference electrode in 0.1 M $HClO_4$ ($H_2{}^{18}O$ solution). Next, the electrodes were thoroughly rinsed with unlabelled water, flush dried with N_2 and allowed to rest overnight. Then, the electrode was placed into the 'A cell' design of the Hiden Analytical HPR40 differential electrochemical mass spectrometer. Baseline readings for mass-to-charge ratio (m/z) values of 2, 32, 34 and 36 were collected until stable before sample measurement. A scan rate of 2 mV s^{-1} was used during testing.

Other characterizations

X-ray diffraction patterns were acquired using a Rigaku Ultima diffractometer with Cu Kα radiation. Inductively coupled plasma optical emission spectra measurements were carried out using a Thermo iCap7600 analyser. X-ray photoelectron spectra were measured using a Thermo Scientific ESCALAB 250Xi spectrometer.

DFT calculations

All periodic spin-polarized DFT calculations were performed using the Perdew–Burke–Ernzerhof exchange–correlation functional[42], a plane-wave basis set with a cut-off kinetic energy of 500/400 eV for bulk/surface calculations and the projector-augmented wave method as implemented in the Vienna ab initio simulation package (v.5.4.4)[43,44].

Projector-augmented wave pseudopotentials were selected according to the Materials Project database[38]. The electronic convergence criterion was 10^{-4} eV, while the force criterion for geometry relaxation was 0.05 eV $Å^{-1}$. Gamma-centred k-point grids of $50/a \times 50/i \times 50/c$ and $20/a \times 20/b \times 1$ with non-integer values rounded up to the nearest integer were used for bulk and slab calculations, respectively. In all of the slabs, the bottom half of the slab in the vertical z direction was constrained at the bulk positions, while the top half of the slab and the adsorbed species were fully relaxed. The slabs were separated in the perpendicular z direction by 12 Å of vacuum, and a dipole correction was applied. All crystal structure manipulations and data analyses were carried out using the Python Materials Genomics (pymatgen) library[45] and the atomic simulation environment package[46].

Gibbs free energy calculations

Gibbs free energy correction values for reference gas-phase and adsorbate species ($\Delta G_{species}$) were calculated using equation (4):

$$\Delta G_{species} = \Delta ZPE + \int_0^{298.15} C_p \, dT - T\Delta S. \quad (4)$$

The zero-point energy (ΔZPE), the heat capacity (C_p) and the entropy (ΔS) terms were calculated using vibrational frequencies to a temperature (T) of 298.15 K. Ideal gas approximation and harmonic approximation were used for the calculations of gas phase species and adsorbed species, respectively. The Gibbs free energies of OER intermediates were then calculated using the $\Delta G_{species}$ values and added to the calculated DFT electronic adsorption energies, similarly to the previous work by Gunasooriya and Nørskov[6].

Bader charge calculations

Atomic charges were calculated using Bader analysis as implemented by Henkelman and colleagues[47]. We applied a fast Fourier transform grid that was twice as dense as the standard fast Fourier transform grid to ensure that the Bader charge results were fully converged. Effective Bader charges were defined as $q = Z_{val} - q_{Bader}$, where Z_{val} is the number of valence electrons determined from the POTCAR input file and q_{Bader} is the computed Bader charge.

Data availability

All data are available from the authors upon reasonable request.

Code availability

All code used for this work is available from the authors upon reasonable request.

References

1. Seh, Z. W. et al. Combining theory and experiment in electrocatalysis: insights into materials design. *Science* **355**, eaad4998 (2017).
2. Nong, H. N. et al. Key role of chemistry versus bias in electrocatalytic oxygen evolution. *Nature* **587**, 408–413 (2020).
3. Ben-Naim, M. et al. Understanding degradation mMechanisms in $SrIrO_3$ oxygen evolution electrocatalysts: chemical and structural microscopy at the nanoscale. *Adv. Funct. Mater.* **31**, 2101542 (2021).
4. Lin, C. et al. In-situ reconstructed Ru atom array on α-MnO_2 with enhanced performance for acidic water oxidation. *Nat. Catal.* **4**, 1012–1023 (2021).
5. Li, A. L. et al. Enhancing the stability of cobalt spinel oxide towards sustainable oxygen evolution in acid. *Nat. Catal.* **5**, 109–118 (2022).
6. Gunasooriya, G. T. K. K. & Nørskov, J. K. Analysis of acid-stable and active oxides for the oxygen evolution reaction. *ACS Energy Lett.* **5**, 3778–3787 (2020).
7. Wu, Z. Y. et al. Non-iridium-based electrocatalyst for durable acidic oxygen evolution reaction in proton exchange membrane water electrolysis. *Nat. Mater.* **22**, 100–108 (2022).
8. Hao, S. et al. Torsion strained iridium oxide for efficient acidic water oxidation in proton exchange membrane electrolyzers. *Nat. Nanotechnol.* **16**, 1371–1377 (2021).

9. Seitz, L. C. et al. A highly active and stable $IrO_x/SrIrO_3$ catalyst for the oxygen evolution reaction. *Science* **353**, 1011–1014 (2016).
10. Diaz-Morales, O. et al. Iridium-based double perovskites for efficient water oxidation in acid media. *Nat. Commun.* **7**, 12363 (2016).
11. Yang, L. et al. Efficient oxygen evolution electrocatalysis in acid by a perovskite with face-sharing IrO_6 octahedral dimers. *Nat. Commun.* **9**, 5236 (2018).
12. Zhang, R. et al. First example of protonation of Ruddlesden–Popper Sr_2IrO_4: a route to enhanced water oxidation catalysts. *Chem. Mater.* **32**, 3499–3509 (2020).
13. Lebedev, D. et al. Highly active and stable iridium pyrochlores for oxygen evolution reaction. *Chem. Mater.* **29**, 5182–5191 (2017).
14. Lee, K., Osada, M., Hwang, H. Y. & Hikita, Y. Oxygen evolution reaction activity in $IrO_x/SrIrO_3$ catalysts: correlations between structural parameters and the catalytic activity. *J. Phys. Chem. Lett.* **10**, 1516–1522 (2019).
15. Li, L. et al. Probing electrochemically induced structural evolution and oxygen redox reactions in layered lithium iridate. *Chem. Mater.* **31**, 4341–4352 (2019).
16. Wu, Y. Y. et al. Highly efficient oxygen evolution activity of Ca_2IrO_4 in an acidic environment due to its crystal configuration. *ACS Omega* **3**, 2902–2908 (2018).
17. Li, N. et al. Identification of the active-layer structures for acidic oxygen evolution from 9R-$BaIrO_3$ electrocatalyst with enhanced iridium mass activity. *J. Am. Chem. Soc.* **143**, 18001–18009 (2021).
18. Ma, C. et al. Lanthanides regulated the amorphization–crystallization of IrO_2 for outstanding OER performance. *ACS Appl. Mater. Interfaces* **12**, 34980–34989 (2020).
19. Yang, L. et al. Enhanced iridium mass activity of 6H-phase, Ir-based perovskite with nonprecious incorporation for acidic oxygen evolution electrocatalysis. *ACS Appl. Mater. Interfaces* **11**, 42006–42013 (2019).
20. Retuerto, M. et al. How oxidation state and lattice distortion influence the oxygen evolution activity in acid of iridium double perovskites. *J. Mater. Chem. A* **9**, 2980–2990 (2021).
21. Edgington, J., Schweitzer, N., Alayoglu, S. & Seitz, L. C. Constant change: exploring dynamic oxygen evolution reaction catalysis and material transformations in strontium zinc iridate perovskite in acid. *J. Am. Chem. Soc.* **143**, 9961–9971 (2021).
22. Chen, Y. et al. Lattice site-dependent metal leaching in perovskites toward a honeycomb-like water oxidation catalyst. *Sci. Adv.* **7**, eabk1788 (2021).
23. Chen, Y. B. et al. Exceptionally active iridium evolved from a pseudo-cubic perovskite for oxygen evolution in acid. *Nat. Commun.* **10**, 572 (2019).
24. Yun, T. G. et al. Surface dissolution and amorphization of electrocatalysts during oxygen evolution reaction: atomistic features and viewpoints. *Mater. Today* **58**, 221–237 (2022).
25. Wan, G. et al. Amorphization mechanism of $SrIrO_3$ electrocatalyst: how oxygen redox initiates ionic diffusion and structural reorganization. *Sci. Adv.* **7**, eabc7323 (2021).
26. Song, C. W., Suh, H., Bak, J., Bae, H. B. & Chung, S. Y. Dissolution-induced surface roughening and oxygen evolution electrocatalysis of alkaline-earth iridates in acid. *Chem* **5**, 3243–3259 (2019).
27. Flores, R. A. et al. Active learning accelerated discovery of stable iridium oxide polymorphs for the oxygen evolution reaction. *Chem. Mater.* **32**, 5854–5863 (2020).
28. Lee, S., Lee, Y. J., Lee, G. & Soon, A. Activated chemical bonds in nanoporous and amorphous iridium oxides favor low overpotential for oxygen evolution reaction. *Nat. Commun.* **13**, 3171 (2022).
29. Mehta, P., Salvador, P. A. & Kitchin, J. R. Identifying potential BO_2 oxide polymorphs for epitaxial growth candidates. *ACS Appl. Mater. Interfaces* **6**, 3630–3639 (2014).
30. Willinger, E., Massue, C., Schlogl, R. & Willinger, M. G. Identifying key structural features of IrO_x water splitting catalysts. *J. Am. Chem. Soc.* **139**, 12093–12101 (2017).
31. Man, I. C. et al. Universality in oxygen evolution electrocatalysis on oxide surfaces. *ChemCatChem* **3**, 1159–1165 (2011).
32. Deng, X., Chen, K. & Tüysüz, H. Protocol for the nanocasting method: preparation of ordered mesoporous metal oxides. *Chem. Mater.* **29**, 40–52 (2017).
33. Savitzky, B. H. et al. py4DSTEM: a software package for four-dimensional scanning transmission electron microscopy data analysis. *Microsc. Microanal.* **27**, 712–743 (2021).
34. Ravel, B. & Newville, M. ATHENA, ARTEMIS, HEPHAESTUS: data analysis for X-ray absorption spectroscopy using IFEFFIT. *J. Synchrotron Radiat.* **12**, 537–541 (2005).
35. Agrestini, S. et al. Nature of the magnetism of iridium in the double perovskite Sr_2CoIrO_6. *Phys. Rev. B* **100**, 014443 (2019).
36. Sardar, K. et al. Water-splitting electrocatalysis in acid conditions using ruthenate-iridate pyrochlores. *Angew. Chem. Int. Ed.* **53**, 10960–10964 (2014).
37. Li, N. et al. Operando direct observation of Stable water-oxidation intermediates on $Ca_{2-x}IrO_4$ nanocrystals for efficient acidic oxygen evolution. *Nano Lett.* **22**, 6988–6996 (2022).
38. Jain, A. et al. Commentary: the Materials Project: a materials genome approach to accelerating materials innovation. *APL Mater.* **1**, 011002 (2013).
39. Toby, B. H. & Von Dreele, R. B. GSAS-II: the genesis of a modern open-source all purpose crystallography software package. *J. Appl. Crystallogr.* **46**, 544–549 (2013).
40. Juhas, P., Davis, T., Farrow, C. L. & Billinge, S. J. L. PDFgetX3: a rapid and highly automatable program for processing powder diffraction data into total scattering pair distribution functions. *J. Appl. Crystallogr.* **46**, 560–566 (2013).
41. Farrow, C. L. et al. PDFfit2 and PDFgui: computer programs for studying nanostructure in crystals. *J. Phys. Condens. Matter* **19**, 335219 (2007).
42. Perdew, J. P., Burke, K. & Ernzerhof, M. Generalized gradient approximation made simple. *Phys. Rev. Lett.* **77**, 3865–3868 (1996).
43. Kresse, G. & Furthmüller, J. Efficient iterative schemes for ab initio total-energy calculations using a plane-wave basis set. *Phys. Rev. B* **54**, 11169–11186 (1996).
44. Kresse, G. & Furthmüller, J. Efficiency of ab-initio total energy calculations for metals and semiconductors using a plane-wave basis set. *Comput. Mater. Sci.* **6**, 15–50 (1996).
45. Ong, S. P. et al. Python Materials Genomics (pymatgen): a robust, open-source python library for materials analysis. *Comput. Mater. Sci.* **68**, 314–319 (2013).
46. Hjorth Larsen, A. et al. The atomic simulation environment—a Python library for working with atoms. *J. Phys. Condens. Matter* **29**, 273002 (2017).
47. Henkelman, G., Arnaldsson, A. & Jónsson, H. A fast and robust algorithm for Bader decomposition of charge density. *Comput. Mater. Sci.* **36**, 354–360 (2006).

Acknowledgements

This work was partially funded by a National Science Foundation (NSF) CAREER Award (2144365-CBET). This work made use of the Jerome B. Cohen X-Ray Diffraction Facility supported by the MRSEC program of the NSF (DMR-1720139) at the Materials Research Center of Northwestern University and the Soft and Hybrid Nanotechnology Experimental (SHyNE) Resource (NSF ECCS-2025633). This work made use of the EPIC and KECK-II facilities of Northwestern University's NUANCE Center, which has received support from the SHyNE Resource (NSF ECCS-2025633), Northwestern University's

International Institute for Nanotechnology and Northwestern's MRSEC program (NSF DMR-2308691). Research reported in this publication was supported in part by instrumentation provided by the Office of The Director, National Institutes of Health under award number S10OD026871. The content is solely the responsibility of the authors and does not necessarily represent the official views of the National Institutes of Health. Portions of this work were performed at the DuPont–Northwestern–Dow Collaborative Access Team (DND-CAT) located at Sector 5 of the Advanced Photon Source. DND-CAT is supported by Northwestern University, The Dow Chemical Company and DuPont de Nemours, Inc. This research used resources of the Advanced Photon Source, a US Department of Energy (DOE) Office of Science User Facility operated for the DOE Office of Science by Argonne National Laboratory under contract number DE-AC02-06CH11357. We especially thank the assistance from Q. Ma and D. Keane regarding the experimentation at the Advanced Photon Source. The mail-in program at beamline 11-ID-B contributed to the data. The DFT calculations were performed at the OU Supercomputing Center for Education & Research (OSCER) at the University of Oklahoma (OU). G.T.K.K.G. gratefully acknowledges the start-up funding support from the School of Sustainable Chemical, Biological and Materials Engineering at OU.

Author contributions

Conceptualization was by B.L., C.W. and L.C.S. Methodology was by B.L., C.W., X.K.L., G.T.K.K.G., V.D. and L.C.S. Investigation was by B.L., C.W., R.d.R., J.E., R.L., M.E.S., B.R. and G.T.K.K.G. Analysis was by B.L., C.W., R.d.R., J.E., X.K.L., R.L., M.E.S., B.R., G.T.K.K.G. and V.D. Visualization was by B.L., C.W., G.T.K.K.G. and L.C.S. Funding acquisition was by G.T.K.K.G., V.D. and L.C.S. Project administration was by L.C.S. Supervision was by V.D. and L.C.S. Writing (original draft) was by B.L., C.W., G.T.K.K.G. and L.C.S. Writing (review and editing) was by B.L., C.W., R.d.R., J.E., X.K.L., R.L., M.E.S., B.R., G.T.K.K.G., V.D. and L.C.S.

Competing interests

The authors declare no competing interests.

Additional information

Supplementary information The online version contains supplementary material available at https://doi.org/10.1038/s41929-024-01187-4.

Correspondence and requests for materials should be addressed to Linsey C. Seitz.

Peer review information *Nature Catalysis* thanks Hua Zhou, Michal Bajdich, Sung-Yoon Chung and the other, anonymous, reviewer(s) for their contribution to the peer review of this work.